

Energy Storage Systems for Airborne Wind Generators

Bakr Bagaber and Axel Mertens

LEIBNIZ UNIVERSITY HANNOVER

Institute for Drive Systems and Power Electronics

Hannover, Germany

Phone: +49 (0) 511-762-3766

Email: bakr.bagaber@ial.uni-hannover.de

URL: www.ial.uni-hannover.de

Acknowledgments

This work was supported by the German Ministry of Economics and Technology (BMWi) – 0324217D.

Keywords

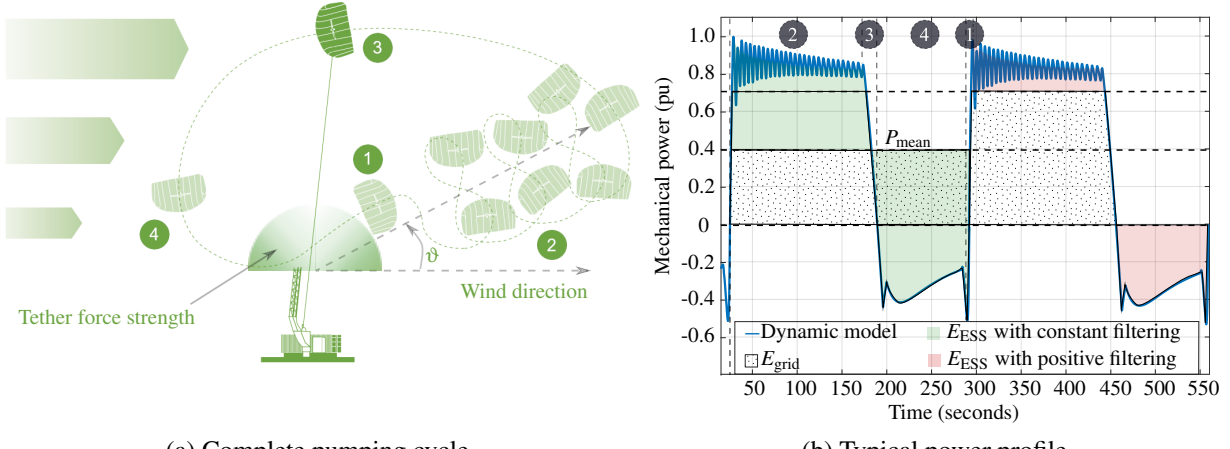
«Wind-generator systems», «Energy Storage», «Flywheel», «Ultra capacitors», «Batteries»,

Abstract

Airborne wind energy systems are known for their volatile output power profile, which can be improved by incorporating energy storage systems for filtering. Lithium iron phosphate batteries, ultracapacitors, and flywheels are compared in this paper under various wind conditions using different power filtering strategies. The comparison considers the energy storage capacity, cost, aging, and reserve storage for ancillary grid services. The results suggest that Lithium batteries have a competitive edge in terms of cost/kWh, whereas steel flywheels provide the cheapest overall solution. The impact of wind turbulence on the system cost was found to be limited. Moreover, reducing the power filtering quality did not contribute to any cost savings. The study also reveals the importance of the holistic cost analysis approach to recognize the trade-offs between savings in the energy storage cost and the rest of the system.

Introduction

Airborne wind energy systems (AWES) are a new class of wind generators promising to harness wind at high altitudes above 200 meters in a cost-effective way [1]. Several concepts of AWES are under research, among which the pumping cycle (PC) type has already reached a market commercialization stage [2]. The system consists of a flying soft kite connected to a ground-based electrical machine by means of a strong tether; a control pod attached to the kite is used for steering. The principle of operation can be understood with the help of Fig. 1a. The cycle is initialized by positioning the kite at a suitable altitude against the wind direction in phase one. In phase two, reel-out (generation) starts by maneuvering the kite in a crosswind direction at a certain wind window angle (ϑ). The crosswind principle exploits the lift-to-drag ratio (E) to induce high apparent wind speed -and lift force- which maximizes the extraction of power [3]. Once the tether is almost entirely winched out, the third phase starts (transition phase). The kite is steered towards the zenith position ($\vartheta = 90$). During this transfer phase, the machine decelerates rapidly towards zero while the torque remains high. Eventually, the fourth phase (reel-in) begins. The electric machine accelerates as a motor to pull the kite into lower elevations. Reel-in is usually accomplished under maximum speed at extensive angles ($\vartheta > 90$) to reduce the tether force. This unique load cycle produces varying output power, as depicted in Fig. 1b, which brings about serious challenges regarding the thermal cycling and lifetime of the machine-side converter [5]



(a) Complete pumping cycle.

(b) Typical power profile.

Fig. 1: principle of operation of a typical PC-AWES: (1) Start/restart, (2) Reel-out (generation), (3) Transfer (generation), (4) Reel-in (consumption), (modified from [4]). The power is normalized to the nominal reel-out power. The shaded area represents the ESS capacity requirements; the dotted area represents the energy transferred directly to the grid.

and compatibility with existing grid codes [6]. Additionally, due to the low inertia of the kite system, it is highly affected by wind gusts which could cause up to 50% overloads during the reel-out phase. The grid-side converter should therefore be over-dimensioned to handle up to 8 times the average cycle power P_{mean} , especially under high wind conditions.

The previous study [6] solved the grid conformity issue by incorporating an energy storage system (ESS). The sizing of two different ESSs, namely lithium iron phosphate (LFP) batteries and ultracapacitors (UC), was conducted for different scenarios. It was found that LFP batteries are more cost-effective than UC in fulfilling the fault ride-through (FRT) requirements. The ESS was also sized for filtering the power injected into the grid. It was concluded that LFP batteries are also better suited than UC for this purpose, although they had to be oversized due to their limited charging currents. However, the previous investigation was based on an average mathematical model for the kite, and it considered only ideal power curves under constant wind speed, as shown in Fig. 1a. Furthermore, the aging mechanisms of the ESS were not considered. In this work, the previous study is extended by using a detailed dynamic model of the AWES and the incorporation of aging models for the ESSs.

On the one hand, LFP batteries are characterized by their high energy density, moderate power density, and operational lifetime. On the other hand, UC are known for their outstanding high power density and cycle lifetime, but they suffer from much lower energy density than lithium batteries and they cost much more [7, 8]. Therefore, alternative ESS, namely flywheels, are also considered in this work. A Flywheel energy storage (FWES) system possesses trade-off characteristics between LFP batteries and UC. They have a slightly better energy density than UC and a comparable power density to LFP [7]. Their cost is also relatively lower than UC, and depending on the application, they could provide a lower cost/cycle count than LFP batteries, making them particularly suitable for AWES [7].

The first section of this paper presents a quick introduction to the system model. An explanation of the investigation methodology then follows. The system sizing results with different power filtering strategies and wind conditions are discussed afterward. Finally, the key findings are summarized.

System Modeling

This section describes the modeling approach of the AWES, the electrical drive, and the ESS in detail.

Pumping Cycle AWES Model

The dynamic model of the pumping cycle AWES can be explained with the help of Fig. 2. The kite position is described using three state variables in the polar coordinate system, the wind window angle

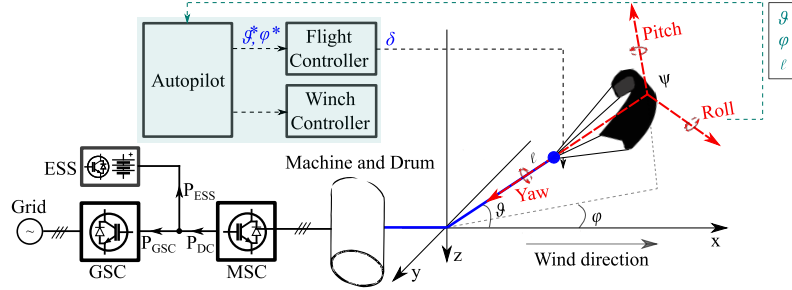


Fig. 2: Overview of the system model.

(ϑ), the azimuth angle (ϕ), and the tether length (l) [9, 3], whereas a fourth state variable (ψ) defines the orientation of the kite around the roll-axis.

Assuming a mass-less kite and the tether in a state of aerodynamic equilibrium with a homogeneous wind field along the x-axis, the dynamic and kinematic equations of motion can be simplified into a first-order system of equations,

$$\dot{\psi} = g_k \cdot v_a \cdot \delta + \dot{\phi} \cdot \cos \vartheta \quad (1)$$

$$\dot{\vartheta} = \frac{v_w}{l} \cdot (E \cdot \cos \vartheta \cdot \cos \psi - \sin \vartheta) - \frac{\dot{l}}{l} \cdot E \cdot \cos \psi \quad (2)$$

$$\dot{\phi} = -\frac{v_w \cdot E \cdot \cos \vartheta - \dot{l} \cdot E}{l \cdot \sin \vartheta} \sin \psi \quad (3)$$

$$\dot{l} = v_{winch}, \quad (4)$$

where (v_w) is the wind speed, (v_a) is the kite's apparent wind speed, and (E) is the glide ratio.

The control system of the AWES comprises a central autopilot, which with the help of a flight controller, defines the optimal flight trajectory of the kite. The steering dynamics are simplified in Equation (1) by the turn-rate law (TRL) $g_k v_a \delta$, where (g_k) is an empirical system parameter that quantifies the maneuvering response of the kite, and (δ) is a non-dimensional control input to the pod controller. A winch controller calculates the optimal winching speed for maximum energy yield according to the method described in [3]. An overview of the kite system parameters is available in Table I.

Modeling the Drivetrain

The electrical machine and the machine-side converter (MSC) are modeled by their rated efficiencies according to Table I.

Modeling the Energy Storage System

The LFP battery equivalent circuit model (ECM) is depicted in Fig. 3a; the model is based on the work of [11]. The model can be described as follows,

$$U_t = U_{oc}(SoC, T) - I \cdot [R_s(SoC, T, SoA) + ZARC(SoC, T, SoA)] \quad (5)$$

$$SoC = SoC_0 - \frac{1}{Q(I, T, SoA)} \cdot \int_0^t I \cdot dt, \quad (6)$$

where (U_{oc}) is the open-circuit voltage of the battery cell, (R_s) is the series resistance representing the ohmic losses, (ZARC) is the complex impedance of the cell represented by a resistor and a parallel constant phase element, (Q) is the cell's capacity, (I) is the cell current, (SoC) is the state of charge, and (U_t) is the cell's terminal voltage. All the equivalent-circuit parameters are either function of the SoC , the state of aging (SoA), and the temperature of the cell core (T). The core temperature is calculated

Table I: System Parameters. The reference cost for the LFP battery, the UC, and the composite FWES is available in [8]. The reference cost for the steel FWES is taken from [10].

Component	Parameter	Symbol	Value	Unit
Kite	Reel-out power	P_{mech}	1.8	MW
	Projected area	A	300	m^2
	Aerodynamic coefficient	C_R	1	-
	Glide ratio	E	5	-
Drivetrain	Winch efficiency	η_{Winch}	95	%
	PMSM efficiency	η_{PMSM}	94	%
	MSC efficiency	η_{MSC}	98	%
	GSC	-	198	$\frac{\$}{\text{kW}}$
LFP cell	Nominal capacity	Q_{nom}	2.5	Ah
	Nominal voltage	U_{nom}	3.3	V
	Discharge current	I_{dis}	70	A
	Max. charging current	I_{char}	10	A
	Rated series resistance (25°C , 80% SoC)	R_s	4.4	$\text{m}\Omega$
	ZARC resistances (25°C , 80% SoC)	$R_{1,2}$	3.7, 218	$\text{m}\Omega$
	ZARC general capacitances (25°C , 80% SoC)	$Q_{1,2}$	8.3, 961	$\frac{\text{s}^n}{\text{m}^2 \cdot \Omega}$
	Power conversion system efficiency	η_{PC}	94	%
	Energy storage cost (now)	-	189	$\frac{\$}{\text{kWh}}$
UC cell	Energy storage cost (in 10 years)	-	96	$\frac{\$}{\text{kWh}}$
	Rated capacitance	C_{nom}	3000	F
	Nominal voltage	U_{nom}	2.7	V
	Max. cont. current	I_{max}	210	A
	Internal resistance	R_{int}	0.29	$\text{m}\Omega$
	Voltage factor	k	917.985	$\frac{\text{F}}{\text{V}}$
	Power conversion system efficiency	η_{PC}	94	%
	Energy storage cost	[8]	32000	$\frac{\$}{\text{kWh}}$
FWES	Steel material density	ρ	7780	$\frac{\text{kg}}{\text{m}^3}$
	Maximum yield strength	σ_{yield}	1.1	GPa
	Shape factor	S	0.3	-
	Poisson's ratio	ν	0.3	-
	Fixed $\frac{r_o}{r_{\text{in}}}$ ratio	-	0.15	-
	Housing thickness	-	0.05	m
	Speed range	-	3-6	kRPM
	FWES efficiency	η_{FWES}	90	%
	Energy storage cost (Composite)	-	37266	$\frac{\$}{\text{kWh}}$
	Power conversion system efficiency	η_{PC}	89	%
	Bearings cost	-	3.45	$\frac{\$}{\text{kWh}}$
	Miscellaneous items cost (of equipment cost)	-	20%	%
Common costs	Vaccume pump cost	-	6000	\$
	Power conversion system (LFP, UC)	-	113	$\frac{\$}{\text{kW}}$
	Power conversion system (FWES)	-	168	$\frac{\$}{\text{kW}}$
	C&C (LFP)	-	96	$\frac{\$}{\text{kWh}}$
	C&C (UC, FWES) of (of equipment cost)	-	20%	\$
	Fixed O&M (LFP, UC, Steel, Composite)	-	8, 1, 6.9, 5.6	$\frac{\$}{\text{kWh-year}}$
	Variable O&M (of annual energy throughput)	-	0.0003	$\frac{\$}{\text{kWh}}$

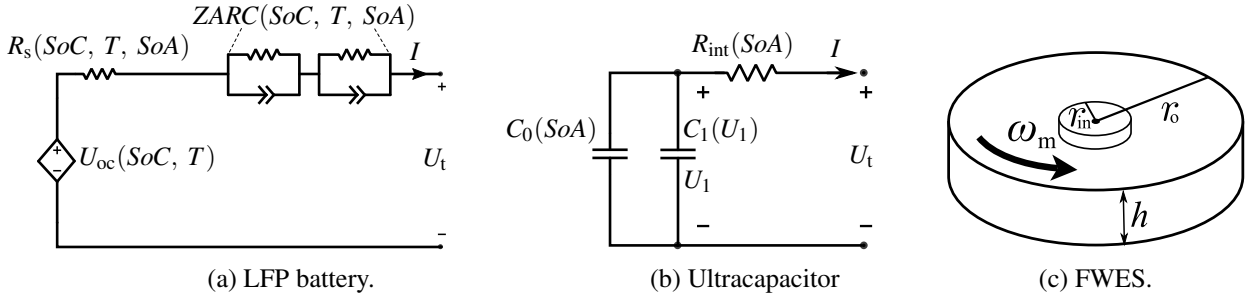


Fig. 3: Model structure of different ESS.

according to [12],

$$T = T_{\text{amb}} + q \cdot R_{\text{th}} \quad (7)$$

$$q = I^2 \cdot R_s(SoC, T, SoA) + I \cdot T \cdot \frac{\partial U_{\text{oc}}}{\partial T}, \quad (8)$$

where (T_{amb}) is the ambient temperature, (R_{th}) is the core-to-ambient thermal resistance of the cell, (q) is the heat dissipation inside the cell, and ($\frac{\partial U_{\text{oc}}}{\partial T}$) is the voltage-temperature coefficient. The first term of Equation (8) represents the joule heat, while the second term represents the reversible heat of the reaction [13]. The reference battery cell parameters are listed in Tabel I.

The degradation of the battery cell is represented by the so-called state-of-aging (SoA) parameter, which combines the calendar and cycle aging mechanisms of each component of the ECM of Fig. 3a independently. According to [11], the SoA can be represented by,

$$SoA_{\text{calendar}} = f(SoC, T, t) \quad (9)$$

$$SoA_{\text{cycle}} = f(SoC, T, DoD, NC) \quad (10)$$

$$SoA = SoA_{\text{calendar}} + SoA_{\text{cycle}}, \quad (11)$$

where (t) is the storage time, (DoD) is the depth of discharge, and (NC) is the number of cycles. The detailed aging equations have been dropped out for conciseness; the reader can refer to [11] for a more comprehensive discussion.

The UC ECM is depicted in Fig. 3b according to the modeling approach in [14, 15]. The governing equations are,

$$U_t = U_1 - I \cdot R_{\text{int}}(SoA) \quad (12)$$

$$U_1 = U_{1,0} - \frac{1}{C_0(SoA) + C_1} \int_0^t I \cdot dt \quad (13)$$

$$C_1 = k \cdot U_1 \quad (14)$$

where (C_0) and (C_1) are the fixed and voltage-dependent capacitances, respectively, (R_{int}) is the equivalent internal resistance of the cell, and (k) is the voltage dependency factor. The UC lifetime degradation follows the method described in [16]. This method extends the classical Eyring's law for calendar aging by incorporating the impact of the load current on the aging acceleration. The SoA is therefore expressed as,

$$SoA = e^{\text{Log}(2) \cdot \frac{T - T_{\text{ref}}}{T_0}} \cdot \left(e^{\text{Log}(2) \cdot \frac{U_t - U_{t,\text{ref}}}{U_{t,0}}} + B \right) \cdot e^{n_{\text{RMS}} \cdot \frac{\bar{I}_{\text{RMS}}}{C_0} \cdot t}, \quad (15)$$

where (B) is a correction factor for low SoC high storage temperature T condition, (n_{RMS}) is the acceleration factor, and (\bar{I}_{RMS}) is the average RMS current over one complete load-cycle. The UC cell temperature can be calculated similarly using Equation (7). A comprehensive list of the UC reference cell parameters is available in Table I.

Finally, the Flywheel is modeled as a rotating cylinder with a shaft at the center, as depicted in Fig. 3c. The stored mechanical energy (E_m) can be described as,

$$E_m = \frac{1}{4} \cdot \pi \cdot h \cdot \rho \cdot (\omega_{m, \max}^2 - \omega_{m, \min}^2) \cdot (r_o^4 - r_{in}^4), \quad (16)$$

where (r_o , r_{in}) is the cylinder's outer and inner radius, respectively, (h) is the height, (ρ) is the material density, and ω_m is the rotational speed. Whereas the maximum specific energy of the FWES is calculated according to,

$$\frac{E_m}{m} = \frac{S \cdot \sigma}{\rho} \quad (17)$$

where (m) is the cylinder's mass, (S) is the Shape factor, and (σ_{yield}) is the maximum allowable material yield strength, which in this work is selected as the yield strength (σ_{yield}) of the material. The DoD , the disk radius, and the maximum allowed material stress (σ_{max}) influence The FWES's allowable number of cycles before breakdown (N_f) [17, 18] as described below,

$$\text{Log}(N_f) = 11.62 - 3.75 \cdot \text{Log}10(1.45 \cdot e^{-7} \cdot \sigma \cdot DoD^{0.44} - 80) \quad (18)$$

$$\sigma_{max} = \frac{1}{4} [(1-v) \cdot r_{in}^2 + (3+v) \cdot r_o^2] \cdot (\rho \cdot \omega_m^2) \quad (19)$$

where v is Poisson's ratio. Two types of FWES are investigated in this work. The first is a steel alloy FWES selected because of its competitive cost and higher safety. The second is a composite FWES characterized by higher energy density. The FWES parameters are summarized in Table I.

ESS Sizing Methods

Following the modeling approach of the last section, two sizing methods are developed and implemented. The first method is based on optimum sizing of the LFP battery and the UC using a particle swarm optimization (PSO) algorithm. The second methods is for sizing the FWES using an iterative process given specific design rules.

LFP and UC Packs Sizing Method

A battery or an UC pack usually comprises several cells connected in series to build up a specific voltage and in parallel to deliver a certain amount of current. To find the optimum number of series and parallel cells (N_s, N_p) of an ESS, a PSO [19] algorithm is used in this work. It is a population-based optimization algorithm for finding the global optima of a given problem under certain constraints.

The multi-objective optimization problem can be described by the following general form [15],

$$\begin{aligned} & \text{Minimize} && f_{\text{obj}}(Z, \zeta) \\ & \text{Subject to} && H_{e,i}(Z, \zeta) = 0, \quad i = 1, 2, \dots, N_e \\ & && H_{ine,j}(Z, \zeta) \leq 0, \quad j = 1, 2, \dots, N_{ine}, \end{aligned} \quad (20)$$

where (ζ) is the input vector, (Z) is the optimization variable vector, (f_{obj}) is the objective function to be minimized, ($H_{e,i}$) and ($H_{ine,j}$) are the i -th and j -th equality and inequality constraints, respectively. The following has been considered,

$$\begin{aligned} f_{\text{obj}} &= \min(N_s \cdot N_p) \\ \zeta &= [P_{DC}] \\ Z &= [N_s, N_p, SOC_0] \\ H_{e,i} &= [\text{Lifetime}] \\ H_{ine,j} &= [E_{ESS} \geq E_{min}, 10\% \leq SoC \leq 100\%, \dots \\ &\dots, I_{cell} \leq |I_{max}|, U_t \leq U_{t, max}, 400 \text{ V} \leq U_{DC} \leq 750 \text{ V}], \end{aligned} \quad (21)$$

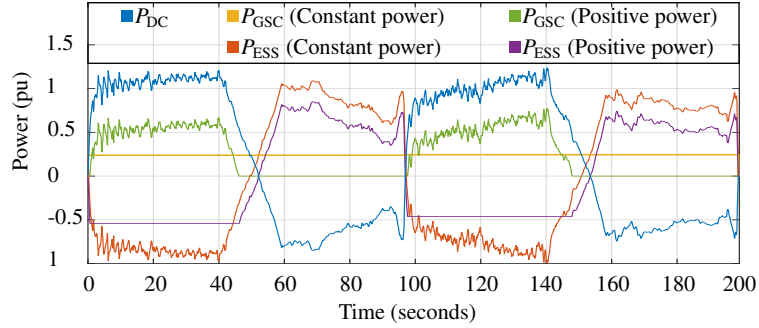


Fig. 4: Power profile of the GSC and the ESS under different power filtering strategies for an average wind speed of $14 \frac{m}{s}$ in open land conditions (c_1). The values are normalized to the average reel-out power.

where (E_{ESS}) is the ESS capacity, and (E_{\min}) is the minimum capacity to meet the power filtering requirements. In order to accelerate the convergence of the solution, the system ordinary differential equations (ODE) describing the LFP and UC models are solved using the forward Euler numerical integration method with a 20 ms simulation time-step. Furthermore, the complex impedance term of the LFP model (ZARC) is approximated by six RC components following the method in [20]. Based on the estimated ESS capacity, the cost is calculated according to the price suggestions of [8]. The cost of the power electronic DC-DC converter is acquired from personal correspondence with multiple manufacturers.

Flywheel Sizing Method

For sizing the steel alloy FWES, the Equations 16 to 19 are solved iteratively until the design's energy storage and lifetime requirements are fulfilled, given the σ_{\max} and $\frac{r_o}{r_{in}}$ dimensional constraints of Table I. Based on the selected design parameters (cylinder dimension), the FWES's cylinder, shaft, and housing masses are calculated. Finally, the cost is estimated according to the prices suggested in [10]. Regarding the composite material FWES, the cost is calculated based on the estimates found in [8], which are calculated from the rated power and energy capacity of the FWES according to the prices in [8].

Power Filtering Strategies

The sizing of the ESS is carried out for two different power filtering strategies. The goal is to identify the grid power quality's impact on the system's overall cost. The "Constant power filtering" strategy achieved full grid power filtering, where the GSC's power remains constant and equal to the average pumping cycle power. Fig. 1b and Fig. 4 explain the relationship between the GSC and ESS power and energy. This strategy trades off higher P_{grid} quality and smaller-sized GSC with more stress on the ESS power requirements.

The "Positive power filtering" allows the ESS to take only so much energy during the reel-out phase to supply the machine during the reel-in phase. The goal is not to consume any power from the grid and avoid the high energy rates dictated by the grid operators. This strategy trades off the quality of P_{grid} filtering by relatively lower ESS power during the reel-out phase.

ESS Sizing Results

ESS capacity and cost

The average results for different wind conditions and power filtering strategies are depicted in Fig. 5. The first column of grouped bars represents the sizing results for the LFP battery based on the power and energy requirements (P/E) as dictated by the kite's mechanical power and the filtering strategy. The second column represents the LFP sizing if the system is designed to last for ten years, which indicates the capacity results. On the other hand, the battery is expected to be replaced once during the project lifetime of 20 years; the replacement expenditures are included in the system cost taking into account the expected reduction in capital cost of LFP cells ten years from now. The remaining columns represent

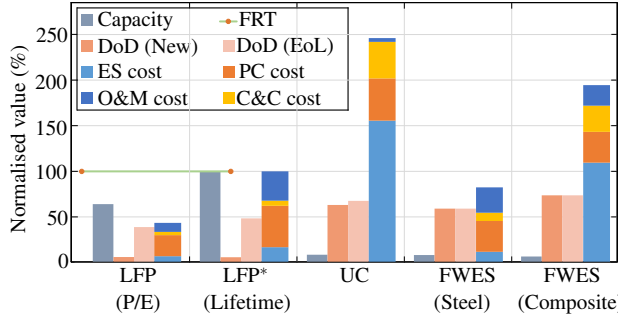


Fig. 5: Energy storage capacity and breakdown of costs for different ESS. The results indicate the average value of different wind conditions and power filtering strategies. Values with an asterisk (*) indicate the base value for normalization. The base value for the capacity is 777 kWh, and 1.23 M\$ for the cost under constant filtering. The DoD is not normalized.

the sizing and cost estimates for the UC and steel and composite material (carbon-fiber) FWES under P/E and lifetime sizing criteria, respectively. Sizing the UC for lifetime was unnecessary since it can inherently withstand many discharge cycles, as will be discussed later in this chapter.

Looking at the results, we can deduce the following. In terms of energy storage capacity, sizing the LFP battery for ten years requires an increase in the capacity by 36% compared to the P/E sizing criteria. However, the sizes of all other ESS are only 8.4%-6.5% of the ten-year LFP battery size. So clearly, the LFP battery needs to be hugely oversized to meet the same P/E and lifetime requirements compared with UC and FWES, primarily due to the LFP's limited power density and feasible cycle count. The ESS capacity also impacts the maximum expected DoD of a newly installed system. The ten-year LFP would have a DoD of only 6%, which leaves plenty of room for additional utilization of the battery capacity for other purposes, such as providing frequency response support for the grid. On the contrary, the DoD for the UC and FWES is about 63% on average, which leaves far fewer reserves for supporting the grid.

The total cost of each system is broken down into energy storage (ES) costs, power conversion system (PC) costs, construction and commissioning (C&C) costs, and operation and maintenance (O&M) costs. The ES costs reflect the costs of the electrochemical cells, the battery management system and other ancillary electronics, and the manufacturing of the battery and UC packs. In the case of the FWES, it represents the costs of the rotating cylinder, the shaft, the steel housing, the vacuum pump, and the assembly costs. The PC costs represent the cost of the DC-DC power converter in the case of electrochemical energy storage systems and the cost of a permanent magnet synchronous machine and a three-phase inverter in the case of FWES. The C&C costs represent the installation costs on-site, whereas O&M costs represent the fixed and variable maintenance costs during the 20 years lifetime. The cost of equipment replacement is included in the cost with which it is associated.

Based on this cost breakdown, the expenses of each ESS are evaluated and depicted against each other in Fig.5, from which we can deduce the following. Although overly sized, the lifetime-sized LFP is still 245% cheaper than the UC option and 195% cheaper than the composite FWES solution. The only solution that provides lower costs than the LFP battery would be steel FWES; it is roughly 21 % cheaper. Additionally, the costs of the LFP battery and the steel FWES are governed by PC costs followed by O&M costs. In contrast, the ES costs do not account for more than 17% for the LFP battery and 12% for the steel FWES. These findings agree with the system specifications, which require very high-rated power but much less storage capacity.

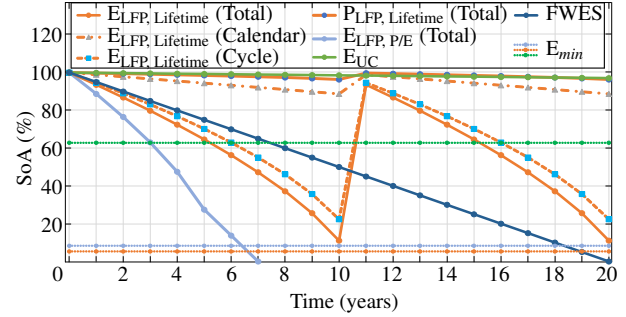


Fig. 6: SoA of different ESS. Capacity and power fade for the LFP and the UC indicate a gradual reduction in performance as the system ages. The FWES SoA indicator only reflects the expected system lifetime assuming the performance remains unchanged.

ESS State of Aging

The comparison between the different ESS is further extended in this section to include aging and performance degradation during the expected project lifetime. Fig. 6 depicts the SoA results as a function of the operational years. The P/E sized LFP total energy capacity fade is depicted in light blue. The capacity drops annually until it reaches the minimum required capacity to fulfill the power filtering goal, roughly after 6.5 years. Therefore, the lifetime sizing was used instead; it is indicated by the solid orange curve, where the LFP capacity approaches E_{min} after ten years before being replaced by another battery pack. The capacity fade is a function of both calendar and cycle aging. In this investigation, the ambient temperature remains constant at 25°C. Therefore the calendar aging contribution is relatively limited, as shown in the figure. On the contrary, the cycle aging mechanism is the main contributor to LFP degradation because of the vast number of annual cycles. The capacity degradation of LFP causes the DoD to increase year after year. Eventually, the DoD could be as high as 49% after ten years, which renders the LFP less helpful in providing ancillary services for the grid towards the end of its lifetime.

Another form of LFP degradation is associated with the pulsed power capability (P_{LFP}) of the cell, as depicted in Fig. 6. This depreciation is, however, limited to no more than 4 %, which means the LFP would still be able to fulfill the fault ride-through requirements of the grid codes even towards the end of its life. The minimum LFP size required to fulfill the FRT (depicted by the green line in Fig. 5) is associated with the limited power density of the LFP and the peak power delivery during grid faults [6]; therefore, the capacity fade is irrelevant in this case as long as the pulsed power capability remains high.

The UC aging is prolonged and mainly contributed by calendar aging, and the capacity drop does not exceed 3% by the end of its lifetime. Here again, the calendar aging is limited by the seamlessly moderate ambient temperature of 25^{circ}C, if higher temperatures were considered, we could expect faster decline rates. The FWES SoA is assumed to be linear, where after 20 years, the accumulated stress on the disk could increase the failure rate. However, unlike the other ESS, the FWES performance is assumed to remain constant during its lifetime and no capacity or power fade is expected.

Impact of Wind Turbulence and Power Filtering Strategy

From the previous discussion, we concluded that LFP batteries and steel FWES are the most competitive candidates for AWES application in terms of capacity and cost. In this section, we try to find out the impact of different wind conditions and power filtering strategies on the overall system cost, including the cost of the ESS and the GSC.

Four different wind conditions [21] are considered in the investigation, and the results are depicted in Fig. 7. Compared with the ideal condition under constant wind speed, the wind turbulence in open land areas (c_1) produces the highest spikes in the kite's output power, it also generates the highest amount of energy, roughly around 18% more than the constant wind condition. The case for agricultural land areas (c_2) generates the next highest values, followed by offshore wind conditions (c_0). The overall system cost follows the power and energy trends; however, the percentage increase in cost is equal to 8% for the LFP and 9% for the FWES compared to the ideal wind condition. The price increase is mainly associated with the cost of the ESS since the GSC only constitutes a small percentage of the overall cost.

The impact of power filtering strategies on the system cost is shown in Fig. 8. Three scenarios are depicted; the first replicates the absence of an ESS, so the overall cost consists of that of the GSC, which has to be sized for the maximum kite power (P_{DC}). The second scenario represents constant output power filtering; the GSC conducts constant power as depicted by the straight yellow line in Fig. 4. Therefore, it is only sized at 13 % of the "No ESS" case. The remaining power has to go through the ESS, as depicted by the red line in Fig. 4. The cost of the ESS plus the GSC is 312% more expensive than that of the "No ESS" scenario for the LFP, and 253% for the FWES.

The positive power filtering strategy results are depicted in the last bar group of Fig. 8. The ESS power and energy demand are slightly less than that of the first strategy. Therefore, the GSC conducts more power and is roughly 300% more expensive than the constant power filtering strategy. It is, however, 37.5% cheaper than without an ESS. Regarding the LFP system cost, although the batteries have to carry

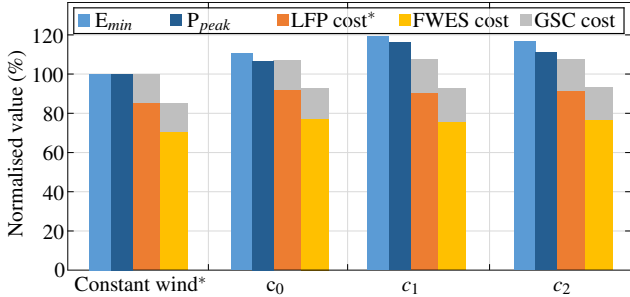


Fig. 7: Impact of wind turbulence on the ESS and GSC loading and cost. The results indicate the average values of different ESS, the GSC, and power filtering strategies.

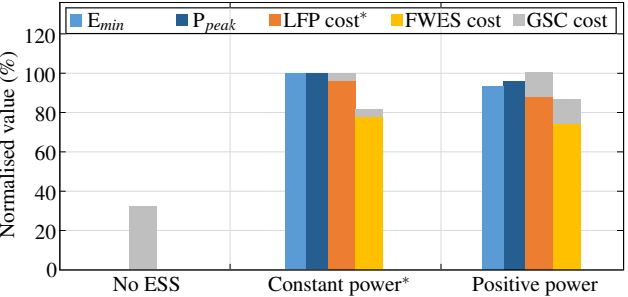


Fig. 8: Impact of power filtering strategy on the ESS capacity and cost. The results indicate the average values of different ESS, the GSC, and wind conditions.

7 % less energy and 4 % less power than the constant filtering case, the overall cost remains unchanged. The cost saving in the LFP system are compromised by the more expensive GSC. The FW case is even more counter intuitive, as one would expect the reduction in the ESS power and energy demand should result in a cost reduction. However, because the energy storage cost constitutes only a fraction of the FW cost, the slight savings achieved are less than the extra costs associated with the oversized GSC. These findings intensify the holistic approach's importance in understanding such a system's cost trade-offs.

Conclusion

This work investigated the sizing of lithium-iron phosphate batteries, ultracapacitors, steel, and composite flywheels for power filtering of pumping cycle airborne wind energy generators. Two power filtering strategies targeting either constant grid power (complete filtering) or positive grid power (partial filtering) were considered. Additionally, the implication of the installation site in terms of different wind classes was also taken into account. The energy storage systems were compared in capacity, usefulness for ancillary grid services, aging/performance impact, and cost.

The results reveal that, on the one hand, lithium-iron-phosphate battery systems provide the lowest cost/kWh at 1690\$/kWh for the complete project, making it the best candidate for installations requiring the provision of ancillary services to the grid. Here, the extra energy reserve can be handy, especially for small island installations where such systems are meant to be used. On the other hand, steel flywheels provide the cheapest cost/kW at 410\$/kW; this is due to the decoupling of the energy storage and power costs for such systems, where the power cost is mainly dictated by the cost of the electrical machine and power electronics converter. They also provide the lowest overall cost, 21% lower than lithium batteries, and they do not suffer from capacity or power fade during their expected lifetime. However, they are much smaller in capacity and do not allow for additional grid services at a competitive cost. The ultracapacitors and composite flywheels are generally 250%-300% more expensive than batteries and thus deemed too expensive for any commercial realization.

The impact of site locations and the associated wind turbulence class was also investigated in this work. The findings suggest that peak power can increase by as much as 19% compared to ideal wind conditions, but the associated cost increase is no more than 8%-9% for batteries and steel flywheels systems. This is because batteries are already oversized to meet the lifetime requirements of the project, so they can inherently withstand higher loads, and the extra cost is linked with oversizing the DC-DC converter system. The case is similar to flywheels, where the extra power only impacts the power conversion system, which has a cost-competitive edge, as discussed earlier.

The power filtering strategy results are even more counterintuitive. One would expect lower power filtering quality to result in cost savings; however, this is not the case. The results indicate that reducing the filtering quality reduces the energy storage system cost. However, it also increases the cost of the grid-side converter. In the case of lithium batteries, it ends up with a similar cost to the constant power filtering strategy, and in the case of the flywheel increases the overall system cost by 6%.

References

- [1] M. Diehl, U. Ahren, and R. Schmehl, *Airborne Wind Energy*. Springer, Berlin, Heidelberg, 2013.
- [2] S. P. GmbH, “Kite Power For Mauritius.” <https://skysails-power.com/kite-power-for-mauritius/>.
- [3] M. Erhard and H. Strauch, “Flight control of tethered kites in autonomous pumping cycles for airborne wind energy,” *Control Engineering Practice*, vol. 40, pp. 13–26, July 2015.
- [4] S. P. GmbH, “SkySails Power GmbH Image Brochure.” <https://skysails-group.com/downloads/>.
- [5] B. Bagaber, P. Junge, and A. Mertens, “Lifetime Estimation and Dimensioning of the Machine-Side Converter for Pumping-Cycle Airborne Wind Energy System,” in *2020 22nd European Conference on Power Electronics and Applications (EPE'20 ECCE Europe)*, Sept. 2020.
- [6] B. Bagaber and A. Mertens, “Fault Ride-Through Performance of Pumping Cycle Airborne Wind Energy Generators with the Support of Optimally Sized Energy Storage System,” in *2021 IEEE 12th Energy Conversion Congress & Exposition - Asia (ECCE-Asia)*, pp. 1144–1150, May 2021.
- [7] X. Luo, J. Wang, M. Dooner, and J. Clarke, “Overview of current development in electrical energy storage technologies and the application potential in power system operation,” *Applied Energy*, vol. 137, pp. 511–536, Jan. 2015.
- [8] K. Mongird, V. Viswanathan, P. Balducci, J. Alam, V. Fotedar, V. Koritarov, and B. Hadjerioua, “An Evaluation of Energy Storage Cost and Performance Characteristics,” *Energies*, vol. 13, p. 3307, June 2020.
- [9] M. Erhard and H. Strauch, “Control of Towing Kites for Seagoing Vessels,” *IEEE Transactions on Control Systems Technology*, vol. 21, pp. 1629–1640, Sept. 2013.
- [10] M. M. Rahman, E. Gemechu, A. O. Oni, and A. Kumar, “The development of a techno-economic model for the assessment of the cost of flywheel energy storage systems for utility-scale stationary applications,” *Sustainable Energy Technologies and Assessments*, vol. 47, p. 101382, Oct. 2021.
- [11] D.-I. Stroe, *Lifetime Models for Lithium Ion Batteries Used in Virtual Power Plants*. PhD thesis.
- [12] C. Forgez, D. Vinh Do, G. Friedrich, M. Morcrette, and C. Delacourt, “Thermal modeling of a cylindrical LiFePO₄/graphite lithium-ion battery,” *Journal of Power Sources*, vol. 195, pp. 2961–2968, May 2010.
- [13] Y. Cai, Y. Che, H. Li, M. Jiang, and P. Qin, “Electro-thermal model for lithium-ion battery simulations,” *Journal of Power Electronics*, vol. 21, pp. 1530–1541, Oct. 2021.
- [14] R. Faranda, M. Gallina, and D. Son, “A new simplified model of Double-Layer Capacitors,” in *2007 International Conference on Clean Electrical Power*, (Capri, Italy), pp. 706–710, IEEE, May 2007.
- [15] A. Ostadi and M. Kazerani, “A Comparative Analysis of Optimal Sizing of Battery-Only, Ultracapacitor-Only, and Battery-Ultracapacitor Hybrid Energy Storage Systems for a City Bus,” *IEEE Transactions on Vehicular Technology*, vol. 64, pp. 4449–4460, Oct. 2015.
- [16] T. Kovaltchouk, B. Multon, H. Ben Ahmed, J. Aubry, and P. Venet, “Enhanced Aging Model for Supercapacitors Taking Into Account Power Cycling: Application to the Sizing of an Energy Storage System in a Direct Wave Energy Converter,” *IEEE Transactions on Industry Applications*, vol. 51, pp. 2405–2414, May 2015.
- [17] X. Li, B. Anvari, A. Palazzolo, Z. Wang, and H. Toliyat, “A Utility-Scale Flywheel Energy Storage System with a Shaftless, Hubless, High-Strength Steel Rotor,” *IEEE Transactions on Industrial Electronics*, vol. 65, pp. 6667–6675, Aug. 2018.
- [18] “Military Handbook: Metallic Materials And Elements For Aerospace Vehicle Structures,” 1998.
- [19] J. Kennedy’ and R. Eberhart, “Particle Swarm Optimization,” p. 7.
- [20] S. Buller and R. W. de Doncker, *Impedance Based Simulation Models for Energy Storage Devices in Advanced Automotive Power Systems*. No. 31 in Aachener Beiträge Des ISEA, Aachen: Shaker, 2003.
- [21] T. Haas and J. Meyers, “AWESCO Wind Field Datasets [Data set],” *Zenodo*, 2019.